PCCP

ARTICLE TYPE

Cite this: DOI: 00.0000/xxxxxxxxxx

Towards realistic simulations of polymer networks: tuning vulcanisation and mechanical properties†

Alessio David,[a] Ugo Tartaglino,[b] and Guido Raos*[c]

Received Date
Accepted Date

DOI: 00.0000/xxxxxxxxxx

Simulations of coarse-grained network models have long been used to test theoretical predictions about rubber elasticity, while atomistic models are still largely unexplored. Here we devise a novel algorithm for the vulcanisation of united-atom poly(cis-1,4-butadiene), characterize the topology of the resulting networks and test their mechanical properties. We observe clear deviations in chain dimension when using slower vulcanisation, contrary to the traditional view that cross-linking simply freezes the melt configuration. Non-ideality of our networks reverberates on the distribution of strand length and on the strands deformation, which is highly non-affine, especially for short strands. Nevertheless, we do recover some of the trends observed on ideal bead-and-spring networks and controlled laboratory experiments, such as the linear relationships linking the degree of cross-linking and the density. We also compare different deformation methods and find step-equilibrium protocols to be more reliable. Regardless of the adopted method, it is advisable to precede the deformation by a pre-stretching cycle in order to release internal stresses accumulated during the vulcanisation.

1 Introduction

Rubber and rubber elasticity have been at the core of polymer science since its birth.[1,2] Today, rubber is still considered a paradigm for the behavior of soft matter, thanks to its large and nonlinear mechanical response and the dominant role of entropy in its behavior.[3] Fundamental and applied investigations of rubber elasticity have led to a plethora of empirical and theoretical models that mostly apply to certain materials or to limited deformation regimes. Statistical mechanical models have the advantage of relating materials parameters to structure, guiding the preparation of polymer networks towards the desired properties, but they tend to be limited to idealized situations.[4] Heuristic models are often more universally applicable, but the empirical parameters entering their constitutive equations are difficult to relate to structure.[5,6] Establishing a connection between theory, experiments and applications is also hampered by the difficulties in the molecular-level characterization of the networks.[7,8] Below we briefly discuss the prominent rubber models, in order to establish a notation and set the stage for our own work.

The starting point for any theory of rubber elasticity are the affine[9] and the phantom network[10] models. They both rely on Gaussian, infinitely extensible chain strands connecting the cross-links. They assume that stress arises entirely from the change in the entropy of the network upon deformation, which occurs at constant volume. Under uniaxial deformation, if we define $\lambda = l/l_0$ as the ratio between the deformed and undeformed lengths of the sample in the pulling direction, the cross-section area changes as $A = A_0/\lambda$. In the affine network model, cross-links are rigidly attached to an elastic background that deforms homogeneously, following the macroscopic deformation. In the phantom network model, only a subset of the cross-links (e.g., those at the surface of the sample) are constrained in this way. All the others are allowed to fluctuate and contribute to the stress, by an extent which depends on their functionality ϕ, defined as the number of strands branching from them. Both models lead to the same functional form for the stress-strain relationship. Under a uniaxial extension or compression:

$$\sigma(\lambda) = \alpha \nu k_B T(\lambda^2 - \lambda^{-1}) \quad (1)$$

where the *true* stress is the ratio between the pulling force and the deformed cross-section of the material ($\sigma = F_{\mathrm{deform}}/A$). Using instead the nominal or *engineering* stress, which is the ratio between the pulling force and the undeformed cross-section of the material ($\sigma_{\mathrm{eng}} = F_{\mathrm{deform}}/A_0$), we have:

$$\sigma_{\mathrm{eng}}(\lambda) = \alpha \nu k_B T(\lambda - \lambda^{-2}). \quad (2)$$

The prefactor entering both equation is proportional to the Young modulus of the material, $E = (d\sigma/d\lambda)_{\lambda=1} = 3\alpha\nu k_B T$. It is the product of the thermal energy ($k_B T$, a "signature" of the entropic origin of rubber elasticity), the density of elastically ac-

[a] Department of Chemistry, Materials and Chemical Engineering, "G. Natta", Politecnico di Milano, Milan 20131, Italy
[b] Pirelli Tyre S.p.A., 20126 Milan, Italy
[c] Department of Chemistry, Materials and Chemical Engineering, "G. Natta", Politecnico di Milano, Milan 20131, Italy; E-mail: guido.raos@polimi.it
† Electronic Supplementary Information (ESI) available

tive strands (ν)—loops and dangling ends do not carry stress and therefore are classified as elastically inactive defects—and a factor α that measures the effectiveness of the active strands. This is simply equal to unity in the affine network model, while it is $\alpha = (\phi - 2)/\phi$ in the phantom one. Thus, $\alpha = 0.5$ in a perfect tetrafunctional network, and it converges to unity when $\phi \gg 1$. We see that higher functionalities allow smaller fluctuations, leading back to the affine network result. The modulus of a phantom network can also be expressed as $\xi k_B T$, where ξ is the cycle rank. This describes the number of elastic degrees of freedom and it can be calculated from two definitions that can be shown to be equivalent for perfect networks, where every strand is elastically active:[4]

$$\xi = \nu - \mu_j = \nu\left(1 - \frac{2}{\phi}\right) \tag{3}$$

where μ_j is the number density of junctions.

More elaborate rubber elasticity models have been developed since the 1970's, in order to improve and reduce the strong assumptions underlying the original ones. Major theoretical efforts have concentrated on the inclusion of entanglements—topological constraints that limit the movement of the chains. These act as additional, effective cross-links, causing an increase of the modulus but also deviations from the behavior embodied by equations (1) and (2). In the constrained-junction models[4,11,12], topological constraints are assumed to be concentrated on the cross-links. In the tube models,[13,14] not only cross-links, but all the monomers are attached to the non-fluctuating elastic background, in order to model chains whose movements are constrained to a 'tube'. Within slip-link models[15?], the entanglements are modelled as 'rings' that constrain the fluctuations of two chains passing through them. If the ring can slide up to a distance which is small compared to the distance from another link, it acts as chemical bond and the model reduces to a phantom network with a higher cross-link density. In the other case, the rings can pass through each other and the chains can disentangle locally.

While the previous statistical-mechanical models provide fundamental insights, engineering applications tend to incorporate a certain degree of empiricism and data fitting.[6,7] Micromechanical models derive quantities from a strain energy function W, which relates the deformation to the energy stored by the material. The Mooney-Rivlin constitutive law typically reproduces experimental data up to 100% deformation and is based on the strain energy density:[5,16]

$$W = C_1(I_1 - 3) + C_2(I_2 - 3), \tag{4}$$

where C_1 and C_2 are material constants, while

$$I_1 = \lambda_1^2 + \lambda_2^2 + \lambda_3^2 \quad \text{and} \quad I_2 = \lambda_1^2\lambda_2^2 + \lambda_2^2\lambda_3^2 + \lambda_3^2\lambda_1^2 \tag{5}$$

are invariants that are independent of the coordinate system (a third invariant is $I_3 = \lambda_1^2\lambda_2^2\lambda_3^2$, which is unity for a constant-volume deformation).

The stretch ratios λ_i in Eq.(5) describe the deformation along three principal axes. In the case of uniaxial deformation, the stress can be derived through differentiation of the strain energy with respect to the uniaxial strain:

$$\sigma_{\text{eng}} = \left(2C_1 + \frac{2C_2}{\lambda}\right)\left(\lambda - \frac{1}{\lambda^2}\right). \tag{6}$$

To extract C_1 and C_2 from a fit, stress vs. strain data are plotted in the Mooney-Rivlin form, having

$$\sigma^*_{\text{eng}} = \frac{\sigma_{\text{eng}}}{\lambda - \frac{1}{\lambda^2}} \qquad \text{and} \qquad \beta = \frac{1}{\lambda} \tag{7}$$

on the y and x axis respectively. If C_2 is zero, the expression reduces to the so-called neo-Hookean model. This coincides with Eq.(2), but it is built on a micromechanical assumption instead of being derived from a macromolecular picture. Generally, C_1 is said to be connected to the network structure, and in particular to the cross-linking density. C_2 is related to non-permanent constraints, such as entanglements and, in particle-filled systems, filler-filler and filler-polymer contacts.[17] This model, as most of the existing ones, does not include non-Gaussianity effects given by the finite extensibility of chains.

In the 1990s, computational models of networks started to appear[18–21], testing theoretical frameworks and finding molecular explanations to empirical fits. *In-silico* experiments are fully designed by the user: in principle, by selectively changing individual parameters, it is possible to test their contribution to the macroscopic properties.[22] Unlike experiments that give average values over a large ensemble, Molecular Dynamics (MD) and other simulation methods offer the possibility to test statistical models, by giving full access to the microscopic details that enter those averages.[23,24] Unfortunately, this advantage does not come free of costs and the quantities extracted from a simulation suffer from noise and uncertainty. Indeed, the understanding has always been limited by the multiscale nature of macromolecular systems, and rubber networks in particular. The vulcanisation reactions adopted by the rubber industry are complex, as they aim at the optimization of productivity, efficiency and costs.[25] Reaction rate can be controlled by temperature, as well as accelerator ratio and type. High temperature guarantees faster curing, but it also causes some degradation. An increased sulphur content obviously leads to a denser network, but also promotes poly-sulphur connections, that are linked to early aging. The addition of accelerators instead fosters mono- and di-sulphur connections, but worsens the dynamical properties.[26] In addition to chemical defects, networks and gels can also display strong inhomogeneities in the local density of cross-links, depending on the relative rates of chain diffusion and reaction.[27] We also point out that vulcanization is conducted shortly after mixing and extrusion, so that shear stresses may not yet be fully relaxed before they are "frozen-in" by the cross-links.

Clearly, the generation of the network is a critical step also for computational studies. In some cases, this complex step has been overcome by simulating networks with idealized (e.g., diamond-like) connectivities.[28,29] This is advantageous when the aim is to understand of the basic physics of rubber elasticity, but not when trying to simulate the behavior of real materials. In end-linked networks[30,31], a fraction of the chain ends are function-

alised with cross-linkers of functionality f. If the fraction of functionalised ends is f^{-1}, the reaction is stoichiometric and should lead to a network that is free of dangling ends. In reality, towards the end of the process, the slow diffusion of the partially bonded cross-linkers makes it impossible to obtain a fully reacted network. An alternative strategy involves bonding of the chain ends to random monomers within the chains, leading to trifunctional cross-links.[31] Another less conventional path[32] starts from a fixed cross-links configuration, from which to build a network of strands whose length is extracted from the predicted Gaussian distribution. Completely random cross-linking[19] is the method that mostly resembles the real process, but produces a larger number of dangling ends, that may be deleted afterword. Dangling ends do not contribute to the elastic stress, complicating the comparison with the existing theoretical models. Note that most of the studies cited above adopted a generic bead-and-spring model, originating from the work of Kremer and Grest on polymer melts and networks.[33] In this model in is relatively easy to create new bonds, as the equilibrium bond length is close to the distance of closest approach for non-bonded interactions. Instead, non-bonded distances are around twice the bond length within an atomistic model. This can produce strong instabilities in the simulations and must be properly dealt with.[34,35]

The rate of vulcanization is also crucial. Many computational works use instantaneous or near-instantaneous reactions, following Edward's suggestion that cross-linking simply freezes the unperturbed configuration of the chains within the melt.[13] A few studies have tested the effects of this hypothesis. A work on end-linked bead-and-spring chains[30] has confirmed that the network's static properties are not altered by cross-linking and that the new junctions are randomly dispersed. Regarding the kinetics, they registered a $t^{-0.5}$ time dependence for the concentration of unreacted ends, which is connected to their diffusion according to the Rouse model. In contrast, in a later atomistic work,[34] polymer strands were found to contract in response to vulcanisation. The authors attributed this deviation from ideality to the non-Gaussian behaviour of the shorter strands.

Computational work on networks has recently moved to more complex problems, such as networks with unusual topologies[36] and aging, which involves bond scission and formation.[37,38] Transient bond scission and formation are relevant also for networks showing toughness and self-healing properties, whose behaviour is yet to be formalised.[39–41] Defects and non-uniformity of the cross-link distribution have also been scrutinized,[42? ,43] and they have have been linked to strongly non-affine deformation and stress concentration.[44] Finally, the role of reinforcing nanoparticles within rubber networks has also been addressed, using a variety of models.[24,45–49] All these problems call for constant updating of well-established models, in order to predict mechanical, thermal and degradation behaviour more reliably.

In this work we introduce and study a near-atomistic model of a cross-linked elastomer. We describe in detail a novel computational protocol to build rubber networks with sulphur bridges, and we characterize their properties as a function of vulcanisation density and rate. The chosen polymer is poly(cis-1,4-butadiene), which can be produced by Ziegler-Natta catalysis.[50,51] High-cis butadiene rubber is used in tires because of its strength and resistance to fatigue and fracture.[52] In a recent study, we have developed parameters for the interaction of this polymer with hydrophilic and hydrophobic silica surfaces.[53] In the future, we plan to combine them into a fully-fledged model of rubber-silica nanocomposites, including also the possibility of bond breaking and fracture at large elongations.

The paper starts with the description of the chosen model and of the methods used to equilibrate, vulcanise and deform the systems. The results are divided into sections regarding the resulting network topologies, their mechanical properties and thermodynamic considerations. Conclusions follow.

2 Methods

2.1 Model

The model used for poly(cis-1,4-butadiene) suppresses hydrogen atoms by utilising carbon *super*atoms that implicitly take them into account.[54–56] This coarser representation results in slimmer simulations, while preserving important molecular details such as rotational barriers, which a coarser model would not include.[57,58] Compared to an atomistic representation, this model reduces the number of atoms and bypasses electrostatic interactions, bringing a remarkable speed-up. Also, the suppression of hydrogen atoms allows to use a longer integration timestep of 2 fs. Finally, if necessary, reinsertion of the hydrogen atoms to switch to a fully atomistic model is almost trivial.

Vulcanisation involves a complex series of reactions and rearrangements, but we assume that it only involves the reaction between CH_2 units and pre-dispersed S-S dimers. We also exclude the possibility of isomerization of some *cis* bonds to *trans*.[59] Force field parameters for sulphur atoms are taken from OPLS[60] and, following its philosophy, geometric mixing rules are applied for sulphur-carbon non-bonded interactions. In the vulcanisation process, new bonds, angles and dihedral angles are created, but some of them are not parametrised in OPLS, therefore their constants are assigned by analogy with other listed interactions. All force field parameters are collected in the SI.

Our approach is divided into two main steps, covered in the next sections: equilibration of the polymeric melt and vulcanisation (see Figure **??** for a flowchart of the process). All calculations are performed using scripts based on the LAMMPS code (Large-scale Atomic/Molecular Massively Parallel Simulator).[61]

2.2 Equilibration of the polymeric melt

Equilibration of polymer melts has been tackled in the literature in many different ways, and different criteria can be used as indicators of a well equilibrated melt. We follow a procedure similar to the one implemented by Auhl *et al.*[62], that involves the random insertion of chains and gradual activation of excluded-volume interactions.

The initial configuration of our system is generated by randomly placing and rotating copies of a sample chain into a cubic box, whose side lengths are chosen to achieve a density of 0.93 g/cm^3, which is typical for rubbers.[6,63] The sample chain configuration incorporates some conformational disorder and it is gen-

erated with the Materials Studio software.[64] All systems include 100 chains, each 100-mers long (i.e. 400 carbon atoms). In the initial equilibration of the melt, we use a so-called *soft potential*:

$$V_{ij}^{\text{soft}}(r) = A_{\text{soft}}\left[1+\cos\left(\frac{\pi r}{\sigma_{ij}}\right)\right] \tag{8}$$

which is purely repulsive, being truncated at $r = \sigma_{ij}$. During an NVT run, the prefactor A_{soft} grows from 0 to 20, allowing the chains to lose memory of their initial conformation. This potential avoids excessively large forces arising from atom-atom overlaps in the initial configurations, and it speeds up equilibration by allowing the chains to cross each other and to eliminate initial entanglements. According to the Flory theorem, all polymer chains are "unperturbed" in the melt state.[65] Therefore, large scale properties such as their radii of gyration are largely independent of the non-bonded interaction potential (Lennard-Jones or soft).

At the end of this step, the atoms are well dispersed and it is possible to switch to the steeper, standard Lennard-Jones (LJ) potential:

$$V_{ij}^{\text{LJ}}(r) = 4\varepsilon\left[\left(\frac{\sigma_{ij}}{r}\right)^{12} - \left(\frac{\sigma_{ij}}{r}\right)^{6}\right], \tag{9}$$

shifted and truncated at 12 Å. The system is minimised and a 2 ns NPT simulation is run to converge the density and the end-to-end distance of the chains. As a final step, we randomly disperse different concentrations of sulphur dimers and equilibrate for a further 1 ns in the NPT ensemble.

2.3 Vulcanisation

In our simulations, vulcanisation occurs by forming bonds between the sulphur dimers and the CH_2 groups lying within a bond cutoff distance. Our algorithm ensures that the cross-linkers connect different chains, avoiding the formation of loops, which are network defects. To allow a complete vulcanisation, this process is performed in a cyclic fashion with an increasing cutoff distance, scaling linearly from 4 Å in the first cycle to 8 Å in the last one. Even if the cutoff distance is large, the vulcanisation process is rarely complete, due to the restrictions we set (more details in SI.1). As the chains diffuse, the unreacted sulphur atoms would eventually come across the right atom-type, but since diffusion slows down as the reaction proceeds and the unreacted sulphurs are only a small fraction, we decided to leave a few dimers partially bonded. Their amount is quantified in section 3.1.

The vulcanisation is performed under $NP_{\text{aniso}}T$ conditions, where the three orthogonal box sides are updated independently during the simulation, to maintain the target pressure of 1 atm. Large stresses arising from the new bonds may cause the transition from *cis* to *trans* configuration of some double bonds. This issue has been overcome by performing a gentle transition to the bonded configuration, through the creation of a bond with low force constant that quickly grows to the final value. The stiffening of the bond must be performed in a reasonable time, since a too slow stiffening would allow the bonded atoms to drift apart. We run $c_{\text{tot}} = 160$ reaction cycles, alternated by 40-ps-long stiffening intervals. Hence the whole cross-linking process takes 160*0.04 ns = 6.4 ns, which is almost instantaneous in comparison to the experimental time scales. In order to homogeneously distribute the bonding reactions during the cycles, we set a varying reaction probability. New bonds form for only a given fraction of atoms eligible to bind, given the distance criterion. The probability is set to $i/2c_{\text{tot}}$ where i is the cycle progression. We investigated also the role of the reaction rate, by performing one slow vulcanization simulation, In this case the vulcanisation cycles are alternated to 2 ns $NP_{\text{aniso}}T$ simulation, allowing the structure to relax. In this case the vulcanization takes more than 320 ns. More details about the LAMMPS implementation are reported in SI.1 and the relevant code is included in SI.2. LAMMPS data files for these final states, which could be used to replicate the following simulations, are also given separately in the SI.

We analyse the topological structure and mechanical properties for systems differing by number of sulphur dimers and vulcanisation rate. All the systems start from an equilibrated melt of 100 PB chains. Afterwards, 100, 150, 200, 300 sulphur dimers are added and the system is vulcanized using the previously described procedure. We will refer to the systems by $n =$ (no. dimers / no. chains). Therefore $n = 1$, $n = 1.5$, $n = 2$, $n = 3$ represent systems with increasing degree of cross-linking. We use the notation $n = 2s$ to indicate a system with 2 dimers/chain obtained by slow vulcanisation.

2.4 Deformation methods

We compare two step-equilibrium methods which involve multiple steps of non-instantaneous deformation and equilibration. These methods mirror the experimental tests known as 'imposed strain deformation' (stress relaxation) and 'imposed stress deformation' (creep).

In the imposed strain deformation, the box is stretched in successive steps along one direction, keeping its volume constant by an orthogonal contraction. After each stretching step there is a relaxation interval, during which a barostat acts exclusively on the orthogonal directions, to bring the associated stress components to 1 atm. The imposed stress deformation[66] is performed in the $NP_{\text{aniso}}T$ ensemble, where the parallel stress corresponds to the *true stress* defined in the Introduction, while in the other directions is set to 1 atm. Within the imposed stress deformation, we highlight a technical detail regarding a parameter LAMMPS uses to determine the strain energy needed for the box deformation. When the simulation involves large changes in the dimension of the box, the parameter `nreset`—which controls the strain energy update rate—must be set to a reasonably low value (2 ps in our case).

Within both protocols, after each stepwise deformation (or stepwise increase of the stress), successive 1 ns relaxation steps are repeated until a convergence criterion is satisfied. After that, data are collected over a further 1 ns run. In the imposed strain method, the parallel average stress in the last iteration must converge to a tolerance of 1 MPa to the average stress registered in the previous iteration. In the stress-imposed deformation, a tolerance of 2 Å is similarly considered for the parallel side of the box. The upside of step-equilibrium methods is that quantities are measured at equilibrium, so it is easier to evaluate the confi-

dence interval on the outcome quantities. The downside is that they cannot relate to a deformation rate, because they only give information about the final equilibrated structure. Also, the sampling density of the stress/strain curve depends strictly on the number of steps taken.

In addition to the step-deformation methods, we tested the SLLOD algorithm, used in Non-Equilibrium Molecular Dynamics (NEMD) and originally conceived for liquids.[22,67,68] According to this method, the drifting velocity due to the deformation is subtracted before applying the thermostat. LAMMPS' NEMD implementation does not include a barostat, therefore the deformation of the box is imposed on the three directions. We used a set of equations for the deformation of the box that guarantees the conservation of volume, which is equivalent to consider a Poisson ratio equal to 0.5. This approximation is a good assumption for unfilled rubber at the macroscale. The elongation of the box follows the law $\lambda(t) = 1 + r_{\text{deform}} \times \Delta t$, where the deformation rate is $r_{\text{deform}} = 0.1\text{ns}^{-1}$. Therefore it takes 10 ns to deform the box by $\Delta\lambda(t) = 1$. The advantage of this method is that it can relate to a deformation rate, although the ones achievable by MD are very high in comparison to the experimental ones.[69] The printing rate of the thermodynamic information defines the density of points of the stress/strain curve. The reported stress values are corrected by subtracting the average of the perpendicular components:

$$\sigma = \sigma_{/\!/} - \frac{\sigma_{\perp 1} + \sigma_{\perp 2}}{2} \tag{10}$$

In order to eliminate the possible residual stresses due to the vulcanisation, cyclic deformation was applied on system $n = 2s$ using the NEMD method ($r_{\text{deform}} = 0.1\text{ns}^{-1}$). The deformation included two full cycles of linear stretching (up to $\lambda = 1.5$) and return to equilibrium length, and one last stretching ramp. Given the results of this test (section 3.3) we decided to pre-condition every system with a linear cyclic deformation (from $\lambda = 1$ to $\lambda = 2$ and backwards) along each of the three axes. For the production runs, the systems are stretched again along the three box directions using the methods reported above, and the data are averaged to minimise the noise.

3 Results

3.1 Vulcanisation

The formation of new bonds during the vulcanization is reported in Figure 1a. The curve describing the cumulative bond formation is linear until approximately 90% of possible bonds have formed. Without a scaled bond creation probability, the vast majority of bonds would have formed during the first cycles, producing off-equilibrium network models with huge internal stresses, causing the MD simulations to fail after a few time steps. The vulcanisation is complete, i.e. 100% dimers have reacted, for systems with $n > 1.5$, while it saturates at 98.5% and 99.7% for $n = 1$ and $n = 1.5$ respectively.

In theory, instantaneous vulcanisation should produce little changes in the melt configuration. Figure 1b shows that n is linearly connected to the increase in density, as $\rho(\text{g/cm}^3) = 0.97 + 0.01n$. The inset of Figure 1b shows that in the final vulcanised state, more and more non-bonded interactions are replaced by covalent bonds, causing a slight but measurable volume contraction. The initial concentration of sulphur does not cause large differences in the density, nor does the vulcanization rate.

The influence of vulcanisation on the statistical properties of the chains can be monitored through their radii of gyration R_{g} and the end-to-end distances R_{ee}. Figure 1c reports their values before ($n = 0$) and after the vulcanisation. For sufficiently long, unperturbed chains satisfying random-walk statistics, their mean-square values are related by: $\langle R_{\text{g}}^2 \rangle = \langle R_{\text{ee}}^2 \rangle / 6$.[30] Hence the end-to-end values have been plotted after rescaling by a factor of six. The two quantities do not coincide, but differences are contained and, for the most part, do not seem to depend systematically on cross-linking. We point out that the distributions of values are broad compared to the window shown (error bars are not included). All this could be justified by the relatively short chain lengths, leading to non-Gaussian statistics, and the near-instantaneous vulcanization reactions. However, there is a significant increase of the chain size in the slowly vulcanized system. Thus, polymer relaxation between the cross-linking events tend to produce a certain chain stretching. This disagrees with experimental and computational work on end-linked poly(dimethylsiloxane) networks, which either showed no change[30,70] or some contraction of the chain size.[34] There are many possible reasons for this disagreement, including different chemistries and different models or simulation protocols. Note that here we are considering the size of whole precursor chains, not that of the strands between the cross-links. The two coincide in the case of end-linked networks, but are clearly different in our case. Further work would be needed to fully clarify this issue.

The importance of anisotropic barostatting can be appreciated by calculating the standard deviation on the three orthogonal side lengths during the vulcanisation. This is relatively low for the quickly vulcanised systems, fluctuating around 1 Å independently of n, while it is about 3 Å for the slowly vulcanised system (Figure SI.3). System $n = 2s$ experiences stronger fluctuations because the simulation runs for a longer time. Although the fluctuations are contained, they can cause large stress variations, which are more efficiently eliminated by anisotropic barostatting.

3.2 Topology

The topology of the networks has been analysed through methods of graph theory implemented in Mathematica[71]. In each case we have considered the largest connected component of the system, excluding isolated chains and small, disconnected clusters (see the SI for an illustration). The information extracted from the graphs are (Table 1): cycle rank, number of chains connected to the network (i.e. chains connected to the network with at least one cross-link), average number of cross-links per chain, average number of monomers within strands and dangling chains. The latter has been compared with the theoretical prediction

$$l_s = L/(2n+1) \tag{11}$$

by Grest and Kremer,[33,43] where L is the length of the chains. At large n, the predicted value approximates very well the calculated one, while at small n it overestimates it. The dangling chains are

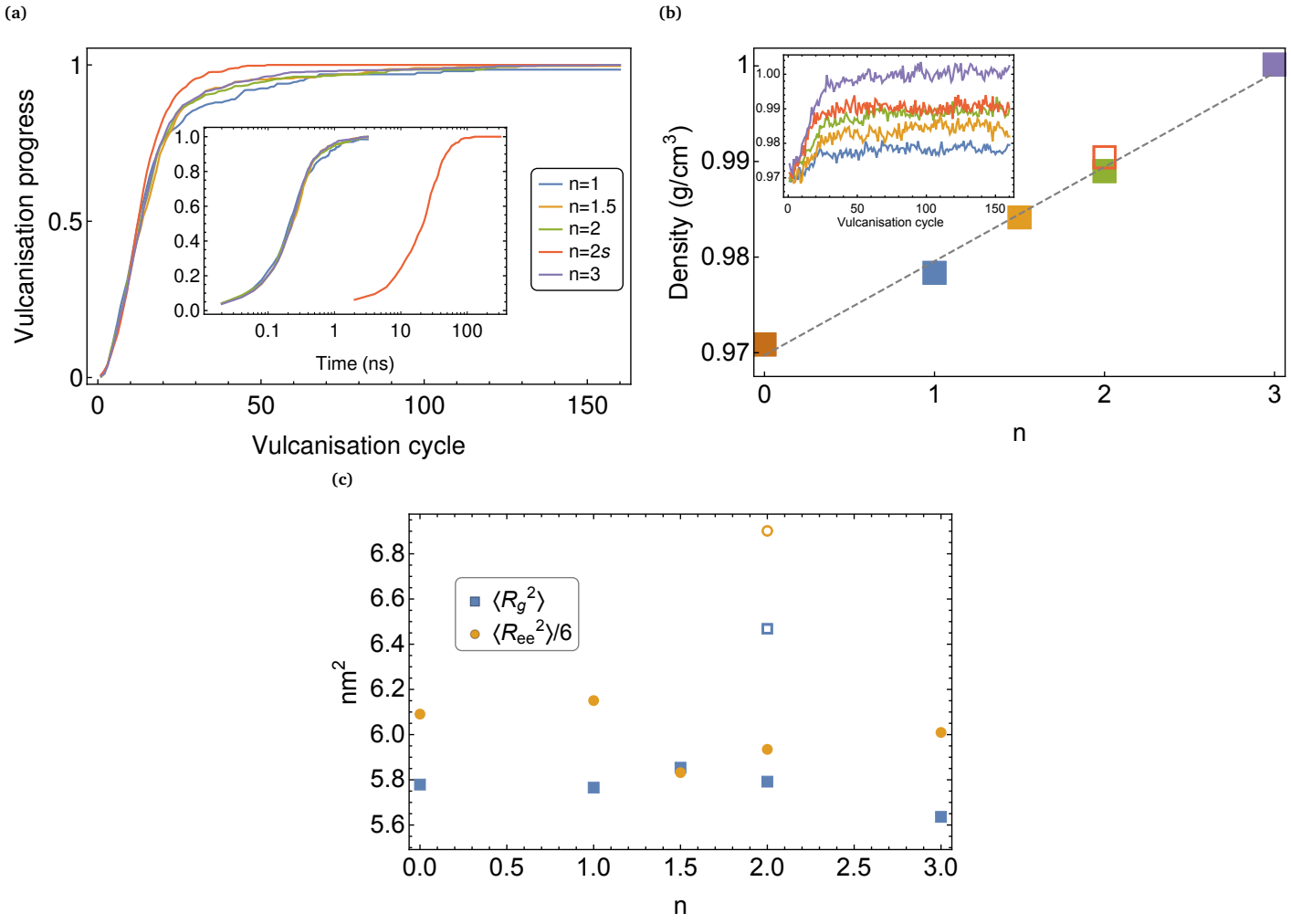

Fig. 1 (a) Vulcanisation progress against vulcanisation cycle. The inset shows the time dependence of the vulcanisation progress. **(b)** Equilibrium density after vulcanisation. Empty symbol refers to system $n = 2s$. The linear fit (dashed) excludes the system $n = 2s$. Inset: density variation with vulcanisation cycle. Colours are self-explanatory. **(c)** Average square radius of gyration and rescaled average square end-to-end distance before ($n = 0$) and after vulcanisation. Empty symbols refer to system $n = 2s$.

shorter than the strands for $n < 2$, while the trend is inverted for higher n. These discrepancies could be connected to the incomplete vulcanisation or to inhomogeneities in the network, as can be appreciated from the number of connected chains. When n is low, a small but significant fraction of chains do not take part in any reaction, and therefore are not included in the subsequent analysis of network structure. The cycle rank has been calculated with the two equivalent definitions of Eq. (3), that should give the same result for perfect networks.[43] Indeed, in our case the values of ξ calculated with the two definitions coincide. The calculated ξ's will be compared to the one coming from the fit of the stress/strain curves in section 3.3.

For random processes, the number of tetrafunctional connections per chain can be represented by a normal distribution centred around $2n$, since each cross-linker connects 2 chains. Figure 2a shows the distributions, rescaled by $2n$. All rescaled plots are centred around unit. System $n = 3$ shows almost perfect symmetry, again demonstrating it best reproduces the predicted theoretical results. As the vulcanisation degree lowers, the distribution is wider and less symmetric. In system $n = 1$, it is skewed and its peak is shifted to lower values. This scenario well reproduces the early results on bead-and-spring networks.[33]

Under the assumption of random cross-linking, the distribution of strand lengths is a simple exponential with decay length equal l_s. Our results are plotted in Fig.2b. The fitted decay length reproduces the values of l_s, except for the system at lowest n. It also overestimates the average strand length, but the error diminished on going to higher n. The decay length is said to approach l_s from below because of the existence of intra-chain loops,[33] which cannot form in our systems.

It is interesting to compare the topologies of systems $n = 2$ and $n = 2s$ and to relate them to their mechanical properties. Average values for the two systems in Table 1 do not differ much. On the contrary, Figure 2a shows that the curve for a slower vulcanisation approaches the ones related to lower n. Instead, the fits of the strand length distributions overlap perfectly. A structural difference is observable in the pair distribution functions $g(r)$ of the S-S dimers and their integrals, which are given in Figures 2c and 2d (distances are measured between the centers-of-mass of the dimers). Before and after quick vulcanisation, the SS dimers are distributed more or less randomly. There is only a slight short-range aggregation, due to the preferential formation of non-bonded contacts among the sulphur atoms. The fast cross-linking almost freezes this situation, apart from a slight enhancement of the peak at contact, while the slow vulcanization leads to a significantly different distribution. In particular, there is a clear tendency of some cross-links to come together and pair up, leaving a depleted shell at distances of 4–8 Å. As we shall see, this can have measurable consequences on the mechanical properties.

3.3 Deformation and mechanical properties

As mentioned in the "Methods" section, vulcanization can produce large local stresses within the polymer, due to the abrupt creation of new chemical bonds. These stresses can be largely eliminated by alternating bond formation and relaxation and allowing anisotropic cell deformations. Nonetheless, the system can still exhibit some residual stresses at the end of the reaction. These can be characterized by performing cyclic deformations.

In a preliminary set of simulations, system $n = 2s$ was stretched from $\lambda = 1.0$ to $\lambda = 1.5$, and then brought back to $\lambda = 1.0$ for three times. The stress history accompanying these deformations is shown in Figure 3a. The first stress ramp lies visibly higher than the others and presents larger fluctuations. The curves for the second and third cycles overlap to a large degree, implying that a sort of equilibrium has been achieved. Nonetheless, even in these cases there is some hysteresis, the stress in the "return" half-cycle being lower than in the previous one. So the system is not purely elastic and there is still some energy dissipation, also due to the high rates of deformation which are employed in the simulations.

Our interpretation is supported by Figure 3b, which presents the torsional energy throughout the cycles. This is the potential energy component which changes more systematically during deformation, when the polymer segments undergo conformational transitions. During the first cycle, some high energy conformations that were locked-in by the vulcanisation are quickly released, and they do not return in the following ones. Given these results, in order to guarantee reproducibility of results, all system were pre-conditioned as described in the “Methods” section.

Figure 4a shows the comparison of the three methods discussed in Section 2.4, from the undeformed state up to $\lambda = 2.0$. The quasi-static creep (imposed stress) and stress relaxation (imposed strain) give comparable results, while the NEMD method tends to produce more noisy data and to predict higher deformation stress. The noise in the data could be readily eliminated by some batch averaging of the stress (implicit in the quasi-static methods), while the higher stress in presumably due to different treatment of volume changes and to the higher deformation rate of the NEMD simulations (the rate $r_{\text{deform}} = 0.1\text{ns}^{-1}$ implies that the system is stretched from equilibrium to $\lambda = 2$ in 10 ns).

Volume conservation is strictly enforced by the non-equilibrium SLLOD equations of motion and, as mentioned in the Introduction, it is indeed assumed to be valid by all the classical theories of rubber elasticity. Instead, the two quasi-static methods allow some volume relaxation, following each deformation step. Volume changes have been reported in Table 2, and they are indeed very small. They can be used to estimate the Poisson ratio ν_P. We did it by a linear fit of $\ln \frac{V}{V_0}$ against $\ln \lambda$, according to the expression:

$$\ln \frac{V}{V_0} = (1 - 2\nu_P) \ln \lambda \tag{12}$$

where V_0 and V are the initial and deformed volume. The data used for the fit refer to the imposed stress method, up to $\lambda = 1.1$, while the stress/strain results for all systems are shown in Figure 4b. The obtained values are indeed slightly less than 0.50 (table 2), as expected.

The two equilibrium methods produce very similar results up to $\lambda = 2$. It is difficult to conclude which of the two is faster and accurate in general, because the convergence criteria act on differ-

Table 1 Topological properties of the networks. One monomer is made of four carbon atoms

n	1	1.5	2	2*s*	3
Connected chains (%)	87	95	99	100	100
Average cross-link per chain (count)	2.3	3.1	4.0	4.0	6.0
Average strand length (mono count)	25.8	22.3	17.7	17.1	14.0
Strand length distribution decaying length (mono count)	28.8	25.8	20.5	20.36	13.7
Average dangling chain length (mono count)	24.7	21.9	21.4	22.4	14.2
l_s **Predicted strand or dangling chain length (mono count)**	33.3	25.0	20.0	20.0	14.3
ξ **Cycle rank (nm^{-3})**	0.012	0.056	0.095	0.095	0.195

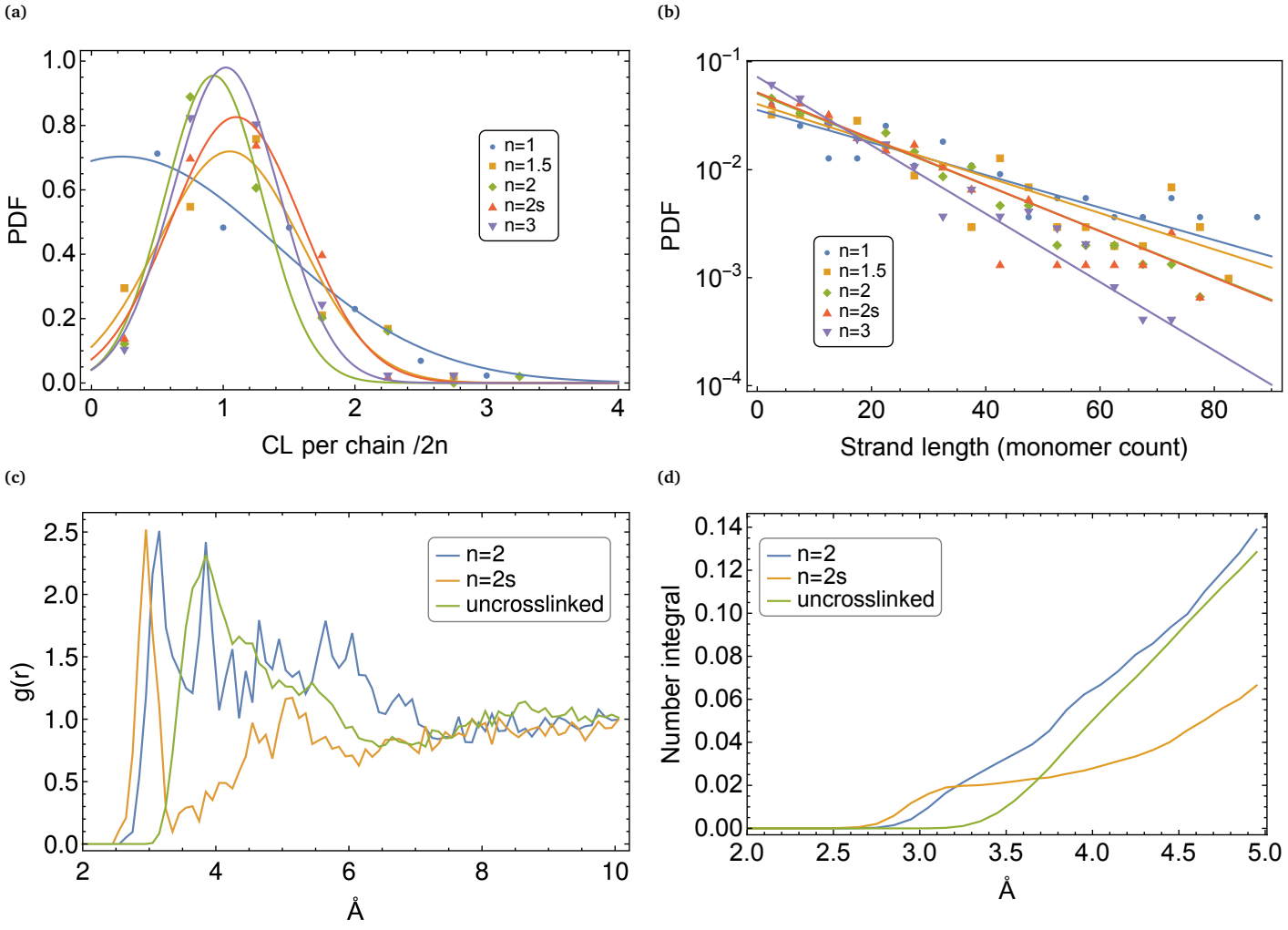

Fig. 2 (a) Probability density function and fit for the number of cross-links per chain. **(b)** Probability density function and fit for the strand length. **(c)** Radial pair distribution function of SS dimers. **(d)** Number integral of the radial pair distribution function of SS dimers (coordination number).

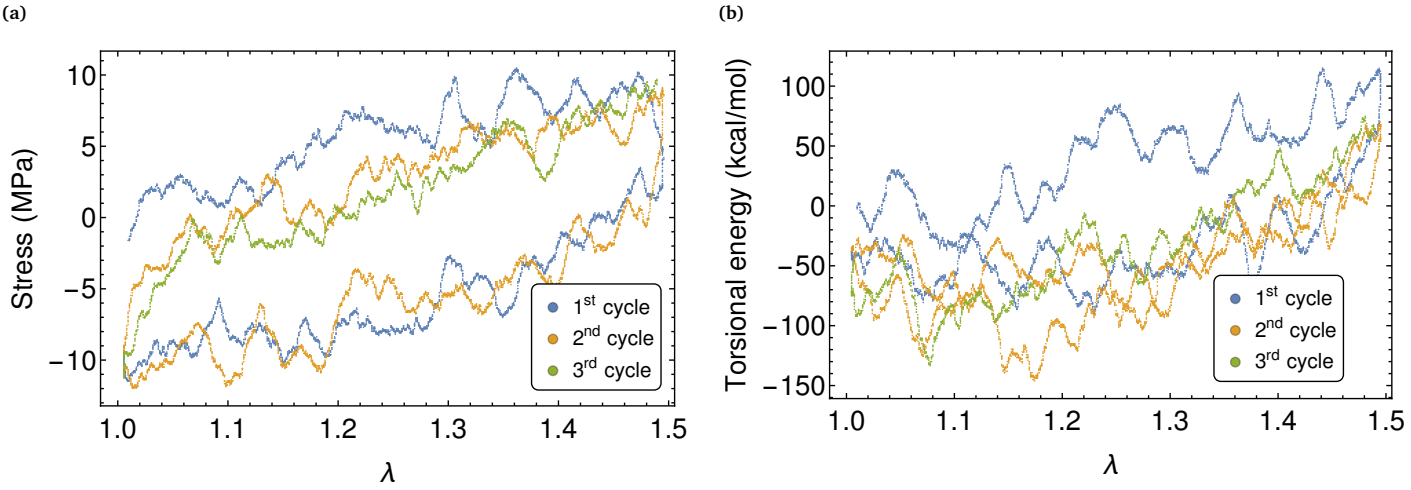

Fig. 3 (a) Stress curves and (b) torsional energy for three deformation cycles of systems $n = 2s$.

ent variables. To calculate the points in Figure 4a the simulation ran for about 75 ns, independently of the method. In this range, the line corresponding to the imposed stress method required 6 points, while the imposed strain method required 5 points.

The data in the range $\lambda = 1.1 - 2.0$ have been fitted with the neo-Hookean model of Eq. (2), in order to extract the $\alpha\nu k_B T$ prefactor. Such prefactor can be identified with the shear modulus G:

$$G = \frac{E}{2(1+\nu_P)} = \frac{1}{3}\left.\frac{d\sigma_{\text{eng}}}{d\lambda}\right|_{\lambda=1} = \alpha\nu k_B T \tag{13}$$

Here E is the Young modulus, a derivative of the stress with respect to the elongation, and $\nu_P = 0.5$ due to incompressibility. Switching to the more general Mooney-Rivlin formula, Equation (6), which comprises the neo-Hooke model as a special case, the shear modulus becomes

$$G = \frac{1}{3}\left.\frac{d\sigma_{\text{eng}}}{d\lambda}\right|_{\lambda=1} = 2(C_1 + C_2) \tag{14}$$

Once G is known, $\alpha\nu$ and α can also be extracted using knowledge of the network structure from Table 1.

Table 2 demonstrates an increase of the elastic moduli with the degree of cross-linking, and a decrease on going to a slowly vulcanized system. After conversion to the α values, these are always well above unity, as predicted by the affine deformation model (the other models would predict even lower values). In the best cases ($n \geq 2$), there is an order-of-magnitude difference theoretical and the simulated moduli. Comparison of the fitted prefactor $\alpha\nu$ (also in Table 2) of Eq. (1) and the calculated ξ (in Table 1), shows that network non-ideality, in addition to entanglements and non-entropic contributions to the stress, causes the theoretical prediction to fail.

In general, the simulated elastic moduli are higher than typical ones coming from experiments on similar networks. The most likely cause of this different is the density of the cross-links. Relative short chains such as those simulated here require higher cross-linking degree to guarantee the formation of a fully-fledged three dimensional network, well beyond the gelation point. Indeed, in the experimental work by Jacobi *et al.* [63], PB chains composed of about 20000 mers were vulcanised to obtain networks of $\xi \approx 10^{-4} nm^{-3}$. This should be compared with $\xi \approx 10^{-1} nm^{-3}$ in our case. Correspondingly, the obtained C_1 and C_2 were about 0.1 MPa. Fits with the Mooney-Rivlin model (Eq. 6) are shown in SI.4 and the extracted C_1 and C_2 values are also reported in Table 2. The last line of the table gives E_{MR}, the estimate of the shear modulus derived from these coefficients according to Equation (14). Comparison with the previous set of G values demonstrates that there is also a certain uncertainty which depends on the choice of the fitting model, but this does not affect the main conclusions derived above.

3.4 Stress per strand

To investigate the local behaviour of the systems, we consider the atomic definition of stress. Within LAMMPS, each atom i contributes to the overall stress according to:[72]

$$s_{\alpha\beta}(i) = -\left[m_i v_{i\alpha} v_{i\beta} + r_{i\alpha} F_{i\beta}\right] \tag{15}$$

where m_i is the atom's mass, and the other quantities are the components of its position, velocity and force ($\alpha, \beta = x, y, z$). Note that $s_{\alpha\beta}(i)$ has the dimension of energy, so it must be divided by a volume to obtain a quantity having the dimension of a stress. Hence, the full stress tensor is then obtained as:

$$\Sigma_{\alpha\beta} = \frac{1}{V}\sum_{i=1}^{N} s_{\alpha\beta}(i)\,. \tag{16}$$

The stress tensor associated with strand a is calculated as a sum over all atoms belonging to it, normalized by the volume of the strand:

$$\sigma^s_{\alpha\beta}(a) = \frac{\sum_{i\in a} s_{\alpha\beta}(i)}{\sum_{i\in a} V(i)} \tag{17}$$

The denominator in the previous equation contains the volumes $V(i)$ associated with the individual atoms, obtained by a Voronoi tessellation.[73,74]

Figure 5 documents the σ^s_{xx} components of the stress of the chain strands, in the direction of elongation. In general, we al-

Table 2 Mechanical properties calculated using the imposed stress deformation

n	1	1.5	2	2*s*	3
ν_P **Poisson's ratio** ($\lambda < 1.1$)	0.49	0.49	0.48	0.49	0.50
$\Delta V/V_0$ (‰) ($\lambda = 1.1$)	1.8	2.3	1.8	1.6	-0.2
G **(MPa)**	4.93 ± 0.56	5.25± 0.99	6.72± 1.11	5.65± 0.75	6.84± 0.46
$\alpha\nu$ **(nm**$^{-3}$**)**	1.20± 0.14	1.28± 0.24	1.63± 0.27	1.37± 0.18	1.66± 0.11
α	10.46± 1.20	5.84± 1.10	3.15± 0.52	4.41± 0.58	5.33± 0.36
C_1 **(MPa)**	-2.78 ± 0.21	-1.64 ± 1.26	-2.12 ± 0.70	-1.09 ± 0.93	0.48 ± 0.62
C_2 **(MPa)**	6.67 ± 0.27	5.79 ± 1.68	7.06 ± 0.89	5.17 ± 1.22	3.80 ± 0.79
G_{MR} **(MPa)**	7.78±0.34	8.30±2.10	9.88±1.13	8.16±1.53	8.56±1.00

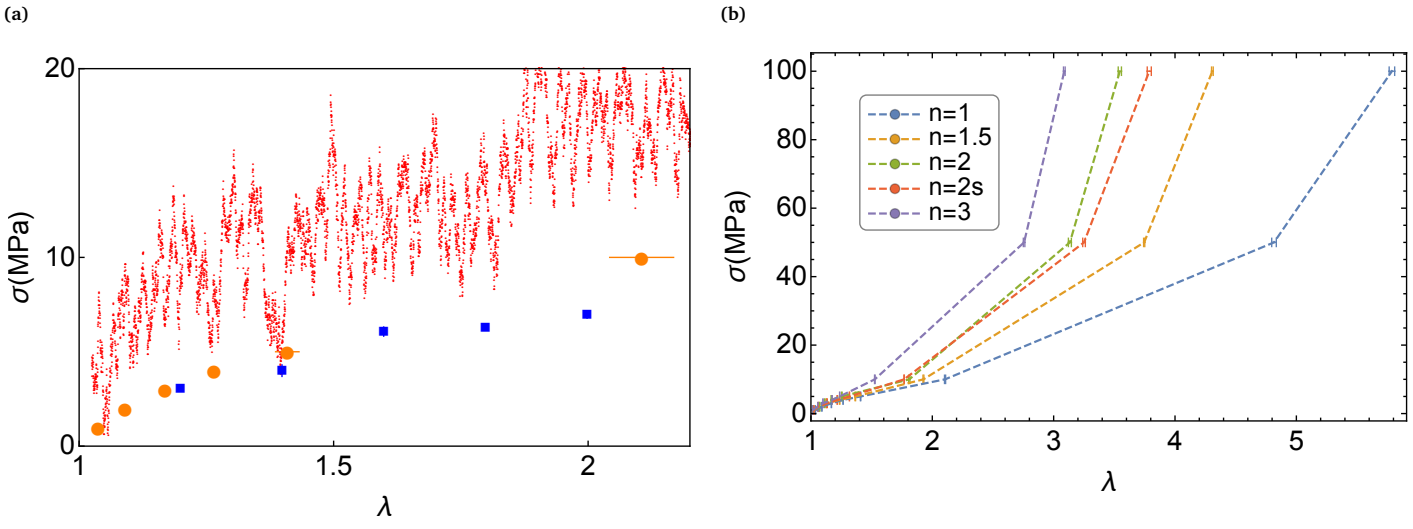

Fig. 4 (a) Comparison between deformation methods for system $n = 1$ in the range $\lambda = 1 - 2$. **(b)** Stress-strain curves for all systems, from the imposed stress deformation.

ways find a broad distribution of stresses, with some chains undergoing compression and and others extension (negative and positive values, respectively). The distribution broadens with the sample elongation. The strands that are subject to the largest stresses (in absolute value) are the short ones, which are also more likely to deviate from ideal Gaussian statistics. They would also be the ones more likely to break, in agreement with our understanding of their role in the rupture and thoughening of polymer networks.[41]

In the work of Gao and Weiner,[18,20] non-bonding interactions are claimed to counterbalance the stress coming from the bonded interactions, by a mechanism named *shielding effect*. This runs contrary to the classic picture of rubber elasticity, according to which the only role of non-bonded interactions is to keep the volume (approximately) constant under deformation. We have calculated the stress per strand originating from the LJ interactions and we see indeed a negative contribution (SI.5). We link this effect to the tendency of chains to maximise the pair interactions as the strands extend.

3.5 Thermodynamics of deformation

In principle, entropy and free energy can be estimated using MD, but their calculation is not trivial as it requires specialized methods to measure the volume of the accessible phase space.[22] These are, in general, computationally very intensive. We report here the results from a simplified method[35] that confirms the entropic origin of rubber elasticity.[3,4] All data in this section derive from the NEMD simulations.

Consider the Helmholtz free energy for a system at constant volume:

$$F = U - TS, \tag{18}$$

where U is the internal energy—readily available from the dynamics—and S is the entropy. Differentiation of F with respect to the box length gives the force, equal in turn to the stress σ times the deformed cross-section A:

$$\sigma A = \left(\frac{\partial F}{\partial l}\right)_T = \left(\frac{\partial U}{\partial l}\right)_T - T\left(\frac{\partial S}{\partial l}\right)_T = f_U + f_S. \tag{19}$$

Here f_U and f_S are respectively forces arising from internal energy and entropy. Thus, the entropic force is calculated as:

$$f_S = -T\left(\frac{\partial S}{\partial l}\right)_T = \sigma A - \left(\frac{\partial U}{\partial l}\right)_T \tag{20}$$

and the variation of entropy ΔS is obtained by integration:

$$\Delta S(l^*) = -\frac{1}{T}\int_{l_0}^{l^*}\left[\sigma A - \left(\frac{\partial U}{\partial l}\right)_T\right] \mathrm{d}l. \tag{21}$$

The data are then rescaled for consistency in the form $\Delta S(\lambda)$. In the process of calculating f_U, data smoothing is applied before differentiation, to avoid noise amplification given by differentiation of a highly fluctuating variable.

Figure 6a shows a comparison between the entropic and enthalpic forces for system $n = 3$. Up to about $\lambda = 3$, the enthalpic force fluctuates around zero, while the entropic force represents the totality of the deformation force, confirming the entropic origin of the elasticity at low to moderate extensions. Figure 6b shows the calculated entropy for all systems. Note that the integration smooths out the fluctuations in the force. In general, the entropy changes are largest for the system with higher degrees of cross-linking.

In order to clarify the role of strand orientation in the entropy change, we include the calculation of the second Legendre polynomial $\mathscr{P}_2[cos\theta]$, where θ is the angle between the end-to-end vector of the strands and the stretching direction. $\mathscr{P}_2$ equals -0.5 for a strand that is orthogonal to the deformation direction, while it is 1 for a strand that is perfectly aligned. Its average $\langle\mathscr{P}_2\rangle$ measures the overall orientation of the system at the strand length scale. An ensemble of randomly oriented strands would give $\mathscr{P}_2 = 0$. Figure 7a shows a non-linear, saturating rise in $\langle\mathscr{P}_2\rangle$ as the deformation proceeds. All systems have overlapping curves, with more dispersed values at lower n. More cross-linked systems have a higher number of strands, and this reduces the fluctuations in resulting average $\langle\mathscr{P}_2\rangle$. It is striking that the orientation of all systems has the same dependence on λ, irrespective of their closeness to the limit of finite extensibility. This occurs earlier for the highly cross-linked systems than for the lightly cross-linked ones (e.g., $\lambda \simeq 3$ for $n = 3$, versus $\lambda > 5$ for $n = 1$). Clearly, in a heterogeneous network in which bonds are not allowed to break, the limit of maximum extensibility will be reached when even a small minority of chains is fully extended. Figure 7b shows a visual representation of the strand orientation for system $n = 2s$ at three different elongations.

4 Conclusions and outlook

We have presented a computational study of the topology and mechanical properties of polybutadiene networks, starting from a detailed description of the methods used to generate them. This methodological part has been made necessary by the adoption of a united-atom model, which is one level of complexity above the widespread bead-and-spring models of rubbers. We have recovered some of the trends observed on ideal bead-and-spring networks and controlled laboratory experiments, such as the linear relationships linking the degree of cross-linking, the elastic moduli and the density. Nonetheless, the simulated moduli are still much higher than typical experimental ones. They are also higher than the predictions of molecular theories based on purely entropic elasticity (for the same network topology). The main reason for this disagreement is likely the relatively short length of the precursor chains (100-mers, or 400 carbons), implying the need of a high concentration of sulphur cross-linker in order to produce a fully developed network. Better quantitative results will come from longer chains and larger system sizes, as well as improvements in atomistic force fields.[75,76]

Traditionally, cross-linking is thought to freeze the melt configuration, while we observed clear deviations in chain dimension when using slower vulcanisation. Both topologically and mechanically, a slower vulcanisation has effects similar to a lowering the cross-linking density. The influence of the vulcanisation velocity has experimental relevance when comparing techniques such as curing by radiation or thermal treatment. Our networks include a large number of defects (broad strand length distribu-

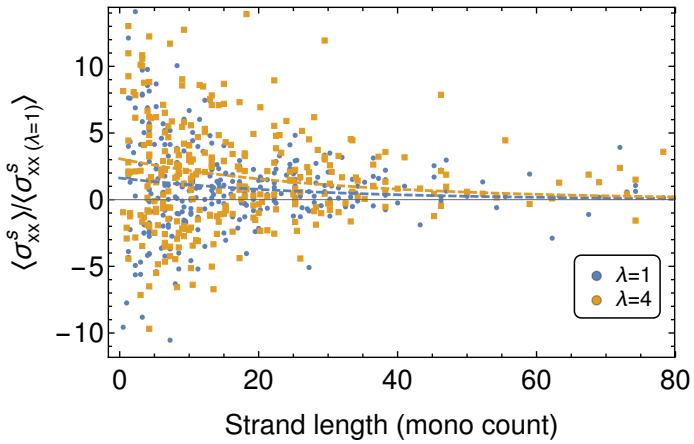

Fig. 5 Normalised stress per strand in the deformation direction vs. strand length for the equilibrium and the stretched state for system $n = 2s$. Exponential trend lines are added.

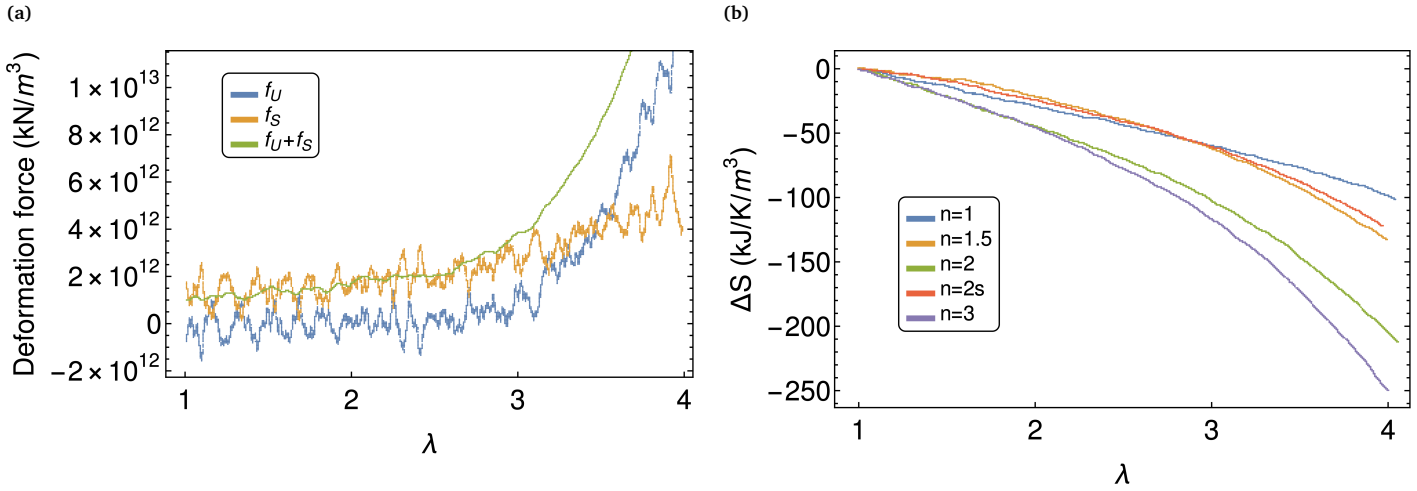

Fig. 6 (a) Enthalpic, entropic and total forces for $n = 3$. **(b)** Entropy variation through the deformation for all systems.

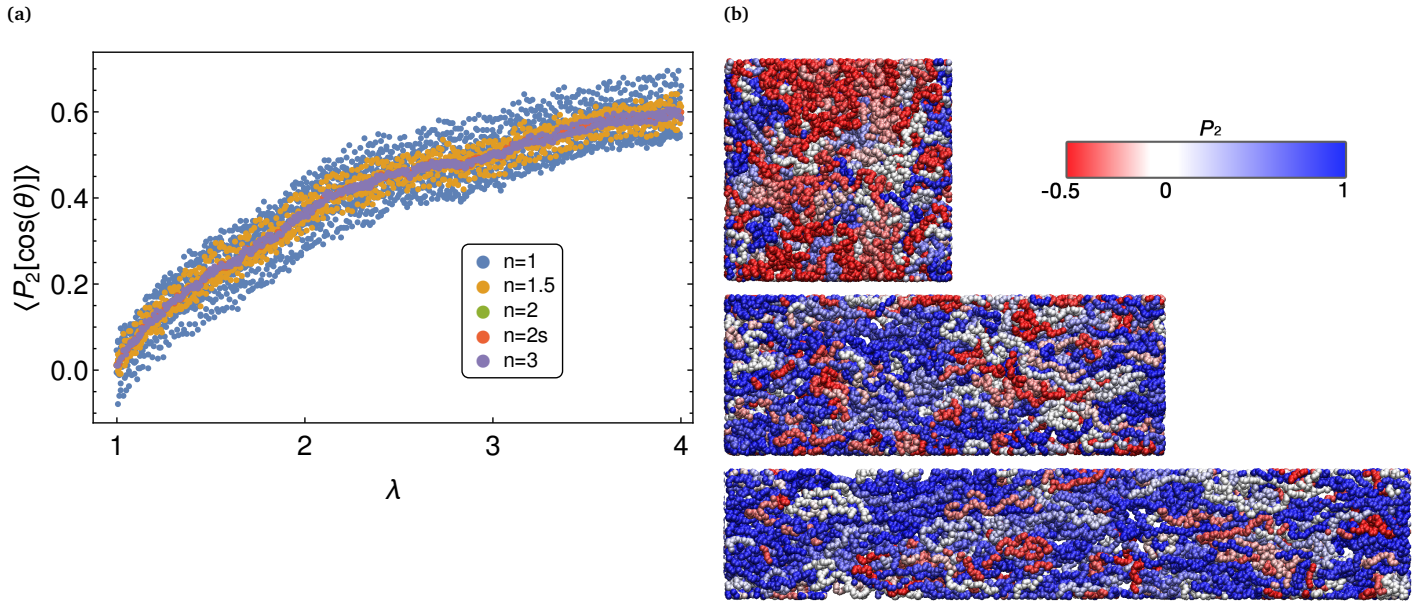

Fig. 7 (a) Average strand orientation parameter $\langle \mathscr{P}_2[\cos\theta] \rangle$ through the deformation. **(b)** Snapshots of the elastically active strands coloured according to their $\mathscr{P}_2[\cos\theta]$ value for system $n = 2s$ at $\lambda = 1, 2, 3$.

tions and presence of dangling chains, but no closed loops), since they are the result of random processes. This reverberates on the strands deformation, which is highly non-affine, especially for short strands.

Pre-stretching cycles are very important for a reliable acquisition of mechanical quantities, in order to release internal stresses and unlock metastable conformations accumulated during vulcanisation. The comparison between deformation methods has shown that the step-equilibrium protocols are more reliable than the non-equilibrium simulations, as implemented in the SLLOD algorithm. Nonetheless, non-equilibrium simulations remain essential when the deformation rate and energy dissipation are relevant variables, such as high-frequency viscoelastic properties and failure at large deformations. A more extensive exploration of non-equilibrium simulations should teach us more about their strengths and weaknesses in these situations. In the meantime, the present and a previous study[53] should provide a good starting point for near-atomistic simulations of reinforcement and toughening of rubber by silica nanoparticles.[77]

Conflicts of interest

There are no conflicts to declare.

Supporting information

Details of LAMMPS implementation and supplementary analyses. LAMMPS data files with force field parameters and structures of the generated networks.

Acknowledgements

This research was funded by Pirelli Tyre S.p.A. and Fondazione Politecnico di Milano under the Pirelli Politecnico di Milano Joint Labs framework.

Notes and references

1 H. Staudinger, *Berichte der deutschen chemischen Gesellschaft (A and B Series)*, 1920, **53**, 1073–1085.

2 V. Abetz, C. H. Chan, C. K. Luscombe, J. B. Matson, J. Merna, T. Nakano, G. Raos and G. T. Russell, *Israel Journal of Chemistry*, 2020, **60**, 9–19.

3 M. Doi, *Soft matter physics*, Oxford University Press, 2013.

4 B. Erman and J. E. Mark, *Structures and properties of rubberlike networks*, Oxford University Press, 1997.

5 L. R. G. Treloar, *Reports on Progress in Physics*, 1973, **36**, 755–826.

6 A. N. Gent, *Engineering with Rubber. How to Design Rubber Components*, Hanser, 2012.

7 B. Basterra-Beroiz, R. Rommel, F. Kayser, S. Westermann, J. L. Valentín and G. Heinrich, *Rubber Chemistry and Technology*, 2017, **90**, 347–366.

8 Y. Gu, J. Zhao and J. A. Johnson, *Trends in Chemistry*, 2019, **1**, 318–334.

9 P. J. Flory and J. Rehner, *The Journal of Chemical Physics*, 1943, **11**, 512–520.

10 H. M. James and E. Guth, *The Journal of Chemical Physics*, 1943, **11**, 455–481.

11 G. Ronca and G. Allegra, *The Journal of Chemical Physics*, 1975, **63**, 4990–4997.

12 P. Flory, *The Journal of Chemical Physics*, 1977, **66**, 5720–5729.

13 S. F. Edwards and T. A. Vilgis, *Reports on Progress in Physics*, 1988, **51**, 243–297.

14 G. Heinrich and M. Klüppel, *Filled elastomers drug delivery systems*, Springer, 2002, pp. 1–44.

15 M. Rubinstein and S. Panyukov, *Macromolecules*, 2002, **35**, 6670–6686.

16 M. C. Boyce and E. M. Arruda, *Rubber Chemistry and Technology*, 2000, **73**, 504–523.

17 U. Eisele, *Introduction to Polymer Physics*, Springer Berlin Heidelberg, Berlin, Heidelberg, 1990, p. 273.

18 J. Gao and J. H. Weiner, *Macromolecules*, 1989, **22**, 979–984.

19 E. R. Duering, K. Kremer and G. S. Grest, *Physical Review Letters*, 1991, **67**, 3531–3534.

20 J. Gao and J. H. Weiner, *Science*, 1994, **266**, 748–752.

21 K. Binder, *Monte Carlo and molecular dynamics simulations in polymer science*, Oxford University Press, 1995.

22 M. P. Allen and D. J. Tildesley, *Computer simulation of liquids*, Oxford university press, 2017.

23 K. C. Jha and M. Tsige, *Rubber Chemistry and Technology*, 2013, **86**, 401–422.

24 S. M. Smith and D. S. Simmons, *Rubber Chemistry and Technology*, 2017, **90**, 238–263.

25 J.-M. Vergnaud and I.-D. Rosca, *Rubber curing and properties*, CRC Press, Boca Raton, 2009.

26 S.-H. Chough and D.-H. Chang, *Journal of Applied Polymer Science*, 1996, **61**, 449–454.

27 F. Di Lorenzo and S. Seiffert, *Polymer Chemistry*, 2015, **6**, 5515–5528.

28 R. Everaers, K. Kremer and G. S. Grest, *Macromolecular Symposia*, 1995, **93**, 53–67.

29 M. Toda and H. Morita, *AIP Advances*, 2018, **8**, 125005.

30 E. R. Duering, K. Kremer and G. S. Grest, *The Journal of Chemical Physics*, 1994, **101**, 8169–8192.

31 G. S. Grest, M. Pütz, R. Everaers and K. Kremer, *Journal of Non-Crystalline Solids*, 2000, **274**, 139–146.

32 D. E. Hanson, *The Journal of Chemical Physics*, 2011, **134**, 064906.

33 G. S. Grest and K. Kremer, *Macromolecules*, 1990, **23**, 4994–5000.

34 D. R. Heine, G. S. Grest, C. D. Lorenz, M. Tsige and M. J. Stevens, *Macromolecules*, 2004, **37**, 3857–3864.

35 R. S. Payal, K. Fujimoto, C. Jang, W. Shinoda, Y. Takei, H. Shima, K. Tsunoda and S. Okazaki, *Polymer*, 2019, **170**, 113–119.

36 S. S. Sheiko and A. V. Dobrynin, *Macromolecules*, 2019, **52**, 7531–7546.

37 D. R. Rottach, J. G. Curro, G. S. Grest and A. P. Thompson, *Macromolecules*, 2004, **37**, 5468–5473.

38 C. Svaneborg, R. Everaers, G. S. Grest and J. G. Curro, *Macromolecules*, 2008, **41**, 4920–4928.

39 T. Matsuda, R. Kawakami, R. Namba, T. Nakajima and J. P. Gong, *Science*, 2019, **363**, 504–508.

40 E. Ducrot, Y. Chen, M. Bulters, R. P. Sijbesma and C. Creton, *Science*, 2014, **344**, 186–189.

41 C. Creton, *Macromolecules*, 2017, **50**, 8297–8316.

42 M. Lang, D. Göritz and S. Kreitmeier, *Macromolecules*, 2003, **36**, 4646–4658.

43 J. Shen, X. Lin, J. Liu and X. Li, *Macromolecules*, 2019, **52**, 121–134.

44 A. A. Gavrilov and A. V. Chertovich, *Polymer Science Series A*, 2014, **56**, 90–97.

45 G. Allegra, G. Raos and M. Vacatello, *Progress in Polymer Science*, 2008, **33**, 683–731.

46 G. Raos and M. Casalegno, *The Journal of Chemical Physics*, 2011, **134**, 054902.

47 Y. Chen, Z. Li, S. Wen, Q. Yang, L. Zhang, C. Zhong and L. Liu, *The Journal of Chemical Physics*, 2014, **141**, 104901.

48 A. S. Pavlov and P. G. Khalatur, *Soft Matter*, 2016, **12**, 5402–5419.

49 K. Hagita, H. Morita, M. Doi and H. Takano, *Macromolecules*, 2016, **49**, 1972–1983.

50 G. Ricci and G. Leone, *Polyolefins Journal*, 2014, **1**, 43–60.

51 Y. Ozawa and T. Takata, *Journal of Applied Polymer Science*, 2019, **136**, 1–8.

52 W. C. White, *Chemico-Biological Interactions*, 2007, **166**, 10–14.

53 A. David, M. Pasquini, U. Tartaglino and G. Raos, *Polymers*, 2020, **12**, 1484.

54 G. D. Smith and W. Paul, *The Journal of Physical Chemistry A*, 1998, **102**, 1200–1208.

55 P. Gestoso, E. Nicol, M. Doxastakis and D. N. Theodorou, *Macromolecules*, 2003, **36**, 6925–6938.

56 L. He, T. D. Sewell and D. L. Thompson, *Journal of Applied Physics*, 2013, **114**, 163517.

57 S. Krushev, W. Paul and G. D. Smith, *Macromolecules*, 2002, **35**, 4198–4203.

58 G. Maurel, F. Goujon, B. Schnell and P. Malfreyt, *The Journal of Physical Chemistry C*, 2015, **119**, 4817–4826.

59 D. Dondi, A. Buttafava, A. Zeffiro, C. Palamini, A. Lostritto, L. Giannini and A. Faucitano, *European Polymer Journal*, 2015, **62**, 222–235.

60 W. L. Jorgensen, J. D. Madura and C. J. Swenson, *Journal of the American Chemical Society*, 1984, **106**, 6638–6646.

61 S. Plimpton, *Journal of Computational Physics*, 1995, **117**, 1–19.

62 R. Auhl, R. Everaers, G. S. Grest, K. Kremer and S. J. Plimpton, *The Journal of Chemical Physics*, 2003, **119**, 12718–12728.

63 M. M. Jacobi, V. Abetz, R. Stadler, L. de Lucca Freitas and W. Gronski, *Colloid and Polymer Science*, 1995, **273**, 544–558.

64 D. S. BIOVIA, *Materials Studio*, https://www.3dsbiovia.com/.

65 P.-G. de Gennes, *Scaling concepts in polymer physics*, Cornell University Press, Ithaca, 1979.

66 D. Brown and J. H. R. Clarke, *Macromolecules*, 1991, **24**, 2075–2082.

67 D. J. Evans and G. P. Morriss, *Physical Review A*, 1984, **30**, 1528–1530.

68 B. D. Todd and P. J. Daivis, *Nonequilibrium molecular dynamics: theory, algorithms and applications*, Cambridge University Press, 2017.

69 H. Yagyu, *Soft Materials*, 2015, **13**, 263–270.

70 M. Beltzung, C. Picot, P. Rempp and J. Herz, *Macromolecules*, 1982, **15**, 1594–1600.

71 W. R. Inc., *Mathematica, Version 12.1*, `https://www.wolfram.com/mathematica`, Champaign, IL, 2020.

72 A. P. Thompson, S. J. Plimpton and W. Mattson, *Journal of Chemical Physics*, 2009, **131**, 1–6.

73 C. H. Rycroft, *Chaos*, 2009, **19**, 2008–2009.

74 G. G. Vogiatzis and D. N. Theodorou, *Macromolecules*, 2014, **47**, 387–404.

75 P. Sharma, S. Roy and H. A. Karimi-Varzaneh, *The Journal of Physical Chemistry B*, 2016, **120**, 1367–1379.

76 A. David, A. De Nicola, U. Tartaglino, G. Milano and G. Raos, *Journal of The Electrochemical Society*, 2019, **166**, B3246–B3256.

77 A. David, *PhD thesis*, Politecnico di Milano, 2020.